Source Shot Noise Mitigation in Focused Ion Beam Microscopy by Time-Resolved Measurement

Minxu Peng^a, John Murray-Bruce^a, Karl K. Berggren^b, Vivek K Goyal^{a,*}

^aDepartment of Electrical and Computer Engineering, Boston University, Boston, MA, 02215, US ^bDepartment of Electrical Engineering and Computer Science, Massachusetts Institute of Technology, Cambridge, MA 02139, US

Abstract

Focused ion beam microscopy suffers from source shot noise – random variation in the number of incident ions in any fixed dwell time – along with random variation in the number of detected secondary electrons per incident ion. This multiplicity of sources of randomness increases the variance of the measurements and thus worsens the trade-off between incident ion dose and image accuracy. Repeated measurement with low dwell time, without changing the total ion dose, is a way to introduce time resolution to this form of microscopy. Through theoretical analyses and Monte Carlo simulations, we show that three ways to process time-resolved measurements result in mean-squared error (MSE) improvements compared to the conventional method of having no time resolution. In particular, maximum likelihood estimation provides reduction in MSE or reduction in required dose by a multiplicative factor approximately equal to the secondary electron yield. This improvement factor is similar to complete mitigation of source shot noise. Experiments with a helium ion microscope are consistent with the analyses and suggest accuracy improvement for a fixed source dose by a factor of about 4.

Keywords: compound Poisson distributions, electron microscopy, Fisher information, helium ion microscopy, Neyman Type A distribution, source shot noise

1. Introduction

State-of-the-art techniques for imaging the structure of a sample at near-atomic resolution depend on the use of microscopes that scan the sample with a focused beam of particles. For instance, a focused electron beam is employed in scanning electron microscopy (SEM) [1], laser beams in confocal laser-scanning microscopy [2] and two-photon laser-scanning fluorescence microscopy [3], and focused ion beams in focused ion beam (FIB) microscopy [4]. A fundamental goal with these technologies is to produce the best image quality for a given number of incident particles. This is especially relevant when each incident particle appreciably damages the sample; because helium ions cause such damage, we henceforth concentrate on helium ion microscopy (HIM) [5].

FIB imaging methods have randomness in the number of incident particles (the *source shot noise*) and in the influence of each incident particle on the device measurement. The goal of the imaging is to infer properties of the sample that are revealed through the number of detected secondary electrons (SEs) per incident ion, and the source shot noise is detrimental to this effort because it is unrelated to the sample. It is intuitive that one would prefer to have a precisely known number of incident ions, and we provide a simple analytical result to demonstrate this in Section 2.2.

The main idea of this work is that time-resolved measurement of SEs can be used to mitigate the effect of source shot

*Corresponding author.

Email address: v.goyal@ieee.org (Vivek K Goyal)

noise. Here, time-resolved (TR) measurement means to divide any given pixel dwell time t into n dwell times t/n and to jointly process the n low-dose measurements to produce one pixel of the micrograph. This type of TR measurement requires no change of hardware: it is a data-processing innovation implemented with existing hardware. The main limitation is whether the dose in dwell time t/n is small enough; roughly, the mean number of incident ions in dwell time t/n should be less than 0.5 to attain at least half of the advantages described herein. Though total dose is not increased, total acquisition time may be increased, depending on the data transfer rate and whether the hardware requires raster scanning to be completed n times to implement this conception of TR measurement.

In certain limiting cases, we can completely eliminate the effect of source shot noise, producing estimation performance equivalent to a deterministic incident ion beam. More importantly, for parameters that reasonably model HIM, the improvement is substantial and validated by both simulations and experiments. While our initial modeling and theoretical results assume direct detection of SEs, our experimental demonstration of improved performance is with extensions of the modeling and algorithms for use with instruments without direct SE detection.

We first presented the TR measurement concept for FIB microscopy in abstract form in [6]. Here, we provide theoretical analyses, develop three estimators for use with TR data, compare these three with the conventional estimator in synthetic simulations, and also compare the best of these estimators with the conventional estimator for experimental data.

1.1. Background

The first image of a solid sample based on secondary electrons emitted in response to an electron beam scanner was produced by Knoll in 1935, inspiring the development of a dedicated SEM [1]. Ever since their development, SEMs have been ubiquitous in both research and industrial imaging, as well as in nanometerological applications [7]. Building upon decades of research in focused ion beam microscopy, the first commercial HIM was introduced in 2006 [5, 8], with the promise of producing images with sub-nanometer resolution [9] and reduced charging of the sample, when compared with SEM. However just like SEM, HIM uses a focused particle beam to produce lateral spatial resolution in a ballistic configuration [5]. Both material composition (e.g., atomic number) and shape (topographic yield variations common to SEM as well) contribute to the number of SEs dislodged from the specimen [10]. These properties, along with improved imaging resolution, larger depth-of-field, and reduced sample charging, have enabled superior imaging of insulators without the need for metal coating. Hence HIM is an important imaging technology for semiconductor and nanofabrication research [11].

Notwithstanding the progress in the pursuit of ultra-high resolution, these imaging technologies all have the disadvantage of causing damage to the sample through sputtering [12, 13, 14]. Whilst sample damage can have especially severe impact on biological samples, it also occurs for many other types of materials. It is thus recognized and modeled as a fundamental limit to imaging with focused beams [13, 15]. With a helium ion being 7300 times more massive than an electron, mitigating sample damage in HIM is paramount. One possible approach is imaging using lower ion doses but at the cost of lower image quality [13]. Consequently, studies analyzing the extent of beam damage and establishing safe imaging dose have appeared [16, 17].

1.2. Outline

In Section 2, we present our baseline Poisson–Poisson measurement model and basic analyses of this model. These analyses provide the foundations for our development, in Section 3, of the advantage provided by dividing any fixed ion dose into small doses through TR measurement. We present both abstract numerical results and image simulations. While a Poisson–Poisson model sufficiently describes direct SE detection, indirect SE detection necessitates additional modeling. Inspired by the indirect detection of SEs in current HIM instruments, Section 4 introduces suitable hierarchical compound models. Section 5 presents experimental results using data from a Zeiss HIM.

2. Single measurement: model and analyses

Two main components enable FIB-based imaging: a stable source to generate the FIB and a detector to measure the number of SEs leaving the sample's surface. Due to ion—sample interaction, SEs become excited and dislodged from the sample's surface [18], accelerating towards the SE detector. Imaging is

achieved by raster scanning the ion beam with some fixed dwell time per pixel. For each pixel, the number of detected SEs is mapped to a grayscale level, hence producing an image of the sample.

During the acquisition process, for any fixed dwell time there is randomness in the number of ions reaching the sample. In addition, for each ion that interacts with the sample, there is randomness in the number of emitted SEs. In this section, we discuss a "Poisson–Poisson" model in which both the numbers of ions and the numbers of SEs induced by each ion follow Poisson distributions, which is a well recognized model in the SEM literature [19]. With this model, the estimability of mean SE yield is amenable to theoretical analysis through Fisher information (FI). The analyses of this section are used to support the use of time-resolved measurement in Section 3, and richer models are considered in Section 4. All the analyses and methods of this paper are applied separately for each micrograph pixel, so we do not include any pixel indexing.

2.1. A Poisson-Poisson model for FIB imaging

In our abstraction, an ion beam incident on the sample for a fixed dwell time t has ion arrivals following a Poisson process with rate Λ per unit time. Hence, the number of incident ions M is a Poisson random variable with mean $\lambda = \Lambda t$. Ion i produces a number of SEs X_i following a Poisson distribution with mean η , i.e., SE yield. Since emitted SEs travel a very short distance before being captured by the SE detector, we model the SE detections as instantaneous and simultaneous. The fundamental assumption is that the delay before SE detection is much less than a typical ion interarrival time; this places some upper limit on the ion beam currents at which our model is reasonable.

The goal is to produce an estimate of η from the total detected SEs

$$Y = \sum_{i=1}^{M} X_i,\tag{1}$$

with known current and dwell time, i.e., λ known. Notice that Y is a sum of M independent Poisson random variables where the unknown M is itself also a Poisson random variable. As shown in Appendix A, Y is an example of a compound Poisson random variable; specifically, it has the so-called *Neyman Type A* distribution [20, 21], with probability mass function (PMF) of detecting y number of SEs

$$P_Y(y; \eta, \lambda) = \frac{e^{-\lambda} \eta^y}{y!} \sum_{m=0}^{\infty} \frac{(\lambda e^{-\eta})^m m^y}{m!},$$
 (2)

mean

$$E[Y] = \lambda \eta, \tag{3}$$

and variance

$$var(Y) = \lambda \eta + \lambda \eta^2. \tag{4}$$

Ward et al. [22] demonstrated empirically that this is an accurate model for numbers of detected SEs in an experimental setup involving a gallium ion beam.

2.2. Conventional estimator

It follows from (3) that simple scaling,

$$\hat{\eta}_{\text{baseline}}(Y) = \frac{Y}{\lambda},$$
 (5)

gives an unbiased estimate of η . The mean-squared error (MSE) of this estimate,

$$MSE(\hat{\eta}_{baseline}) = E\left[(\eta - \hat{\eta}_{baseline}(Y))^{2} \right]$$

$$= \frac{\text{var}(Y)}{\lambda^{2}} = \frac{\eta(1+\eta)}{\lambda},$$
(6)

thus follows from (4). In imaging (in contrast to metrology), the scaling may be arbitrary; thus, when every pixel has the same mean dose λ , the SE counts can be used directly to form a reasonable image.

Assuming for the moment that λ is an integer, if the number of incident ions were deterministically λ , the conventional estimator would be the sample mean of $\{X_i\}_{i=1}^{\lambda}$. Furthermore, it would be the maximum likelihood (ML) estimator of η , it would again be unbiased, and its MSE would be η/λ . The factor of $(1+\eta)$ excess seen in (6) is the cost of the randomness of a Poisson ion beam, i.e., the cost of source shot noise. We will see approximately this factor of improvement from TR measurement, thus approximately cancelling the effect of source shot noise.

2.3. Oracle estimator

If one were able to know M, the estimate

$$\hat{\eta}_{\text{oracle}}(Y, M) = \frac{Y}{M} \tag{7}$$

would be superior to $\hat{\eta}_{\text{baseline}}$ because Y is the sum of M random variables, each with mean η . One can view $\hat{\eta}_{\text{oracle}}$ as mitigating the source shot noise by using the exact number of ions. Along with the issue of resolving 0/0 when no ions are incident, the problem with this is that M is not observable. While the exact number of ions M cannot be known exactly from only observing Y, we will see that M becomes approximately known with TR measurement.

For a non-Bayesian analysis of $\hat{\eta}_{\text{oracle}}$, we can fix an arbitrary value η_0 as the estimate produced when M=0. While $\hat{\eta}_{\text{oracle}}$ is unbiased whenever M>0 (which can be seen by iterated expectation with conditioning on M), there is nothing computable from the data (Y, M)=(0,0) that makes $\hat{\eta}_{\text{oracle}}$ unbiased overall. Specifically,

bias(
$$\hat{\eta}_{\text{oracle}}$$
) = E[$\hat{\eta}_{\text{oracle}}(Y, M)$] - η

$$\stackrel{(a)}{=} \text{E}[\text{E}[\hat{\eta}_{\text{oracle}}(Y, M) | M]] - \eta$$

$$\stackrel{(b)}{=} \eta_0 P(M = 0) + \eta (1 - P(M = 0)) - \eta$$

$$\stackrel{(c)}{=} \eta_0 e^{-\lambda} + \eta (1 - e^{-\lambda}) - \eta$$

$$= (\eta_0 - \eta) e^{-\lambda}, \qquad (8)$$

where (a) follows from the law of iterated expectation; (b) from $E[\hat{\eta}_{oracle}(Y, M) | M = m]$ taking only the values η_0 and η ; and (c)

from the Poisson distribution of M. The variance of the estimate is

$$\operatorname{var}(\hat{\eta}_{\text{oracle}}) \stackrel{(a)}{=} \operatorname{E}\left[\operatorname{var}(\hat{\eta}_{\text{oracle}}(Y, M) \mid M)\right] + \operatorname{var}\left(\operatorname{E}\left[\hat{\eta}_{\text{oracle}}(Y, M) \mid M\right]\right)$$

$$\stackrel{(b)}{=} \eta \sum_{m=1}^{\infty} \frac{1}{m} e^{-\lambda} \frac{\lambda^{m}}{m!} + e^{-\lambda} (1 - e^{-\lambda}) (\eta - \eta_{0})^{2}$$

$$\stackrel{(c)}{=} \eta g(\lambda) + e^{-\lambda} (1 - e^{-\lambda}) (\eta - \eta_{0})^{2}, \tag{9}$$

where (a) follows from the law of total variance; (b) from the conditional distribution of $\hat{\eta}_{\text{oracle}}$ being the constant η_0 for M=0 and the sample mean of $m \operatorname{Poisson}(\eta)$ random variables for M=m, m>0; and (c) introduces a function $g(\lambda)=\sum_{m=1}^{\infty}(1/m)e^{-\lambda}\lambda^m/m!$, which has no elementary closed form. Notice that $g(\lambda)\approx\lambda$ for $\lambda\ll1$, since only the m=1 term is appreciable; moreover, it can be shown that $g(\lambda)\approx1/\lambda$ for $\lambda\gg1$.

The bias and variance computations can be combined to give an expression for the MSE of the oracle estimator:

$$MSE(\hat{\eta}_{oracle}) = [bias(\hat{\eta}_{oracle})]^{2} + var(\hat{\eta}_{oracle})$$

$$\stackrel{(a)}{=} [(\eta_{0} - \eta)e^{-\lambda}]^{2} + \eta g(\lambda) + e^{-\lambda}(1 - e^{-\lambda})(\eta - \eta_{0})^{2}$$

$$= \eta g(\lambda) + e^{-\lambda}(\eta - \eta_{0})^{2}, \qquad (10)$$

where (a) follows by substituting (8) and (9). Furthermore,

$$MSE(\hat{\eta}_{oracle}) \ge \eta g(\lambda),$$
 (11)

with the bound achieved when $\eta_0 = \eta$. We stress that this bound is unachievable because η is not *a priori* known.

2.4. Fisher information

The MSE of any unbiased estimator is lower bounded by the reciprocal of the Fisher information via the Cramér–Rao bound (CRB) [23]. FI is also central to our explanation of why time-resolved measurement combined with ML estimation greatly mitigates source shot noise.

The FI for the estimation of η from Y in the Poisson–Poisson model, with λ a known parameter, can be simplified to

$$I_{Y}(\eta; \lambda) = \mathbb{E}\left[\left(\frac{\partial \log P_{Y}(Y; \eta, \lambda)}{\partial \eta}\right)^{2}; \eta\right]$$

$$= \sum_{y=0}^{\infty} \left(\frac{y}{\eta} - \frac{P_{Y}(y+1; \eta, \lambda)}{P_{Y}(y; \eta, \lambda)} \frac{y+1}{\eta}\right)^{2} P_{Y}(y; \eta, \lambda).$$
(12)

While this expression is not readily comprehensible, it can be used to compute $I_Y(\eta; \lambda)$ numerically and to derive certain useful asymptotic approximations and limits.

One can study $I_Y(\eta; \lambda)/\lambda$ as the information gain per incident ion. This *normalized Fisher information* is a decreasing function of λ , with

$$\lim_{\lambda \to 0} \frac{I_Y(\eta; \lambda)}{\lambda} = \frac{1}{\eta} - e^{-\eta}$$
 (13)

and

$$\lim_{\lambda \to \infty} \frac{\mathcal{I}_Y(\eta; \lambda)}{\lambda} = \frac{1}{\eta(1+\eta)} = \frac{1}{\eta} - \frac{1}{1+\eta}.$$
 (14)

We define a function $\beta(\eta)$ as the ratio of these limits,

$$\beta(\eta) = (1 + \eta)(1 - \eta e^{-\eta}),\tag{15}$$

which varies from 1 to $\approx 1 + \eta$ as η increases from 0. Recall the $1 + \eta$ factor arose in Section 2.2 as the cost of randomness of a Poisson ion beam.

Comparing (14) with (6), we see that, asymptotically for large λ , the conventional estimator achieves the CRB. In contrast, for low λ , the probability for M=0 is appreciable, so there is no (even approximately) unbiased estimator.

3. Time-resolved measurements

Taken together, the analyses in Section 2 suggest that there may be a way for the conventional estimate from (5) to be improved upon to give a reduction in MSE by the factor in (15). TR measurement indeed achieves this improvement. We examine this first through Fisher information and then through simulated performance of the ML estimator for imaging.

3.1. Fisher information of TR measurements

If we divide pixel dwell time t into n sub-acquisitions to obtain Y_1, Y_2, \ldots, Y_n , these are independent and obtained with source dose λ replaced by λ/n . The FI for the set of sub-acquisitions together is

$$I_{Y}^{TR}(\eta; \lambda, n) \stackrel{(a)}{=} n I_{Y}(\eta; \lambda/n)$$

$$= \lambda \frac{I_{Y}(\eta; \lambda/n)}{\lambda/n}$$
(16)

$$\stackrel{(b)}{\approx} \lambda \left(\frac{1}{\eta} - e^{-\eta}\right),\tag{17}$$

where (a) follows from the additivity of FI over independent observations; and (b) holds for large enough n because of (13). Without TR measurement, for total dose values useful for imaging (say, $\lambda > 2$), the limit in (14) provides a good approximation of the FI:

$$I_Y(\eta; \lambda) \approx \lambda \left(\frac{1}{\eta} - \frac{1}{1+\eta}\right).$$
 (18)

The ratio of (17) and (18) was already computed as (15). This ratio gives a convenient way to evaluate the improvement from TR measurement and data processing. The ratio of FIs is the reciprocal of the ratio of Cramér–Rao lower bounds.

3.2. Cramér–Rao bounds

The CRB informs us that no unbiased estimator can have variance lower than the reciprocal of the Fisher information. Thus, the FI for a single measurement (12) and for time-resolved measurement (16) imply bounds on MSE for unbiased

estimators, as plotted in Figure 1. The asymptotic approximation (17) implies a bound that applies to any unbiased estimator $\hat{\eta}_{TR}$ computed from the TR measurements:

$$MSE(\hat{\eta}_{TR}) \ge \frac{\eta/(1 - \eta e^{-\eta})}{\lambda}.$$
 (19)

For the performance without TR measurement, this should be contrasted with (6); the conventional estimator achieves the CRB asymptotically in large λ .

3.3. Quotient mode estimators

When the sub-acquisitions are short enough (that is, n is large enough), each sub-acquisition will have very low dose and thus very likely have 0 or 1 incident ion. Assuming most sub-acquisitions with 1 incident ion yield at least 1 SE, one can use the number of sub-acquisitions with a strictly positive number of detected SEs, i.e. $\sum_{k=1}^{n} \mathbb{1}_{\{Y_k>0\}}$, as a proxy for the number of ions M, where $\mathbb{1}_{\{Y_k>0\}}$ is equal to 1 when $Y_k>0$, otherwise it is equal to 0. Then analogous to the oracle estimator in (7), one can define a *quotient mode* (QM) estimator

$$\hat{\eta}_{\text{QM}} = \frac{Y_1 + Y_2 + \dots + Y_n}{\sum_{k=1}^n \mathbb{1}_{\{Y_k > 0\}}}.$$
 (20)

The QM name is taken from a presentation by John Notte of Zeiss [24] where counting of the analog-domain pulses generated by SE bursts was proposed to give the denominator of an estimator similar to (20). Our QM estimator is implementable with TR measurement, and we improve upon it below and in Section 3.4.

The probability of an incident ion leading to at least 1 emitted SE is $1-e^{-\eta}$, so when the SE yield η is low, $\sum_{k=1}^n \mathbbm{1}_{\{Y_k>0\}}$ becomes a significant underestimate for M, leading to a large bias in $\hat{\eta}_{\text{QM}}$. If we knew η , the adjusted value $(1-e^{-\eta})^{-1}\sum_{k=1}^n \mathbbm{1}_{\{Y_k>0\}}$ would be an improved estimate of M. Since we do not know η , using this improved estimate for M in the denominator of (20) yields a transcendental equation,

$$\eta = \frac{Y_1 + Y_2 + \ldots + Y_n}{(1 - e^{-\eta}) \sum_{k=1}^n \mathbb{1}_{\{Y_k > 0\}}}.$$
 (21)

The solution $\hat{\eta}_{LQM}$ of (21) has the closed form

$$\hat{\eta}_{\text{LOM}} = W(-\hat{\eta}_{\text{OM}}e^{-\hat{\eta}_{\text{QM}}}) + \hat{\eta}_{\text{OM}},\tag{22}$$

where $W(\cdot)$ is the Lambert W function [25]. Hence, we dub $\hat{\eta}_{\text{LOM}}$ the Lambert quotient mode (LQM) estimator.

The QM and LQM estimators are illustrated and numerically assessed in Section 3.5, after we introduce a final estimator.

3.4. Joint distribution and ML estimation

Rather than use the heuristic of dividing the number of detected SEs by an estimate of the number of incident ions, we may apply the statistically principled maximum likelihood approach. For time-resolved measurements, the joint PMF of the vector of observed SEs is

$$P_{Y_1,...,Y_n}(y_1, ..., y_n; \eta, \lambda) = \prod_{k=1}^n P_Y(y_k; \eta, \lambda/n),$$
 (23)

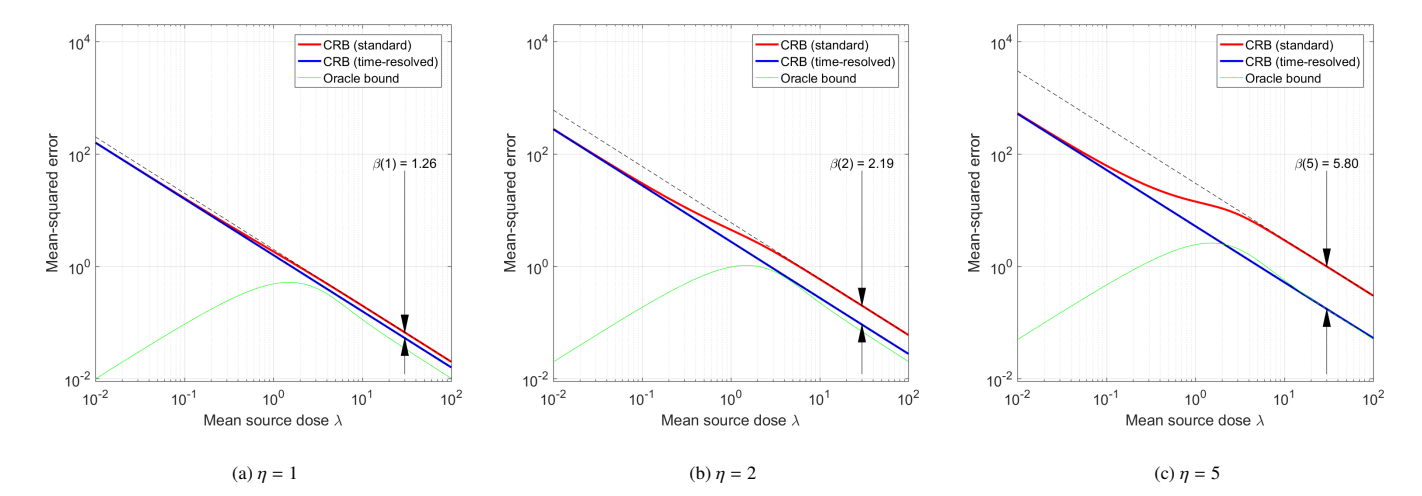


Figure 1: Comparison between the Cramér–Rao bounds obtained for conventional method (red, see (12)) and time-resolved measurement (blue, $n=10\,000$, see (16)) for several values of mean secondary electron yield η . Also shown in each plot is the oracle bound (10) for the estimator (7); recall that this bound is based on estimator that is "increasingly unimplementable" as $\lambda \to 0$ since it is derived from assuming $\hat{\eta} = \eta$ when no ions are incident. Each plot also shows the performance from (6) for the conventional estimate, which is a high- λ asymptote for the Cramér–Rao bound in the case of conventional sensing. The expression (19) is plotted as well, but it lies coincident with the blue curve.

where $P_Y(\cdot;\cdot,\cdot)$ is given by (2). The same expression is called the *likelihood* when viewed as a function of η . Given the TR observation (y_1, y_2, \ldots, y_n) , the *time-resolved maximum likelihood* (TRML) estimate for η is thus

$$\hat{\eta}_{TRML} = \arg\max_{\eta} \prod_{k=1}^{n} P_{Y}(y_k; \eta, \lambda/n).$$
 (24)

Since $\prod_{k=1}^{n} P_Y(y_k; \eta, \lambda/n)$ is a non-convex function of η , we compute the optimization via grid search. This is not prohibitively complex because the decision variable is scalar.

3.5. Comparison of Poisson-Poisson estimators

Note that the QM, LQM, and TRML estimators all exploit TR measurement. Before comparing their performances as η is varied and in imaging simulations, we present a single illustrative example to show how each is computed from a TR observation vector (y_1, y_2, \ldots, y_n) . We also include the unimplementable oracle estimator and the conventional estimator that does not require TR measurement.

Example 1. Consider imaging at a single pixel for which the ground truth is $\eta=2$ with mean total ion dose $\lambda=20$ split evenly over n=100 sub-acquisitions. Figure 2a shows one realization that could occur. The top panel shows the (unobserved) sequence of incident ions $(m_1, m_2, ..., m_{100})$ and the bottom panel shows the sequence of (observed) detected SEs $(y_1, y_2, ..., y_{100})$. Notice that the relatively unlikely possibility of more than one incident ion in a sub-acquisition occurs once, in the 16th sub-acquisition (P $(Y_i > 1) = 1 - e^{-\lambda/n} - \frac{1}{2}(\lambda/n)e^{-\lambda/n} \approx 0.099$). Also, a few times, an incident ion results in no detected SEs.

(i) Oracle. The oracle estimator (7) divides the total number of observed SEs $y = y_1 + y_2 + \cdots + y_{100} = 49$

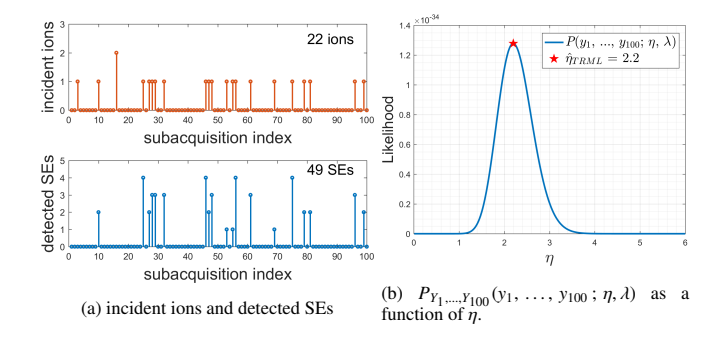


Figure 2: One realization incident ions M and observed SEs Y over n=100 sub-acquisitions with total ion dose $\lambda=20$. The ground Truth $\eta=2$. (a) Stem plot of ions and SEs over sub-acquisition indexes. (b) Joint probability and the TR estimator $\hat{\eta}_{TR}=2.2$ computed from (24).

by the number of incident ions M=22, which yields $\hat{\eta}_{\text{oracle}}(Y,M)=Y/M=49/22\approx 2.23$. However, we emphasize that we do not expect M to be known exactly with any current instrument.

- (ii) Conventional. The conventional estimator (5) divides the total number of observed SEs $y = y_1 + y_2 + \cdots + y_{100}$ by the expected number of incident ions, $\lambda = 20$, which yields $\hat{\eta}_{baseline} = 49/20 = 2.45$. The implicit assumption is that λ is a good estimate for M.
- (iii) **Quotient mode.** The QM estimator (20) divides the total number of observed SEs y by the number of sub-acquisitions with at least one detected SE, i.e., $\sum_{k=1}^{n} \mathbb{1}_{\{y_k>0\}} = 19$, which yields $\hat{\eta}_{QM} = 49/19 \approx 2.58$. Implicitly, $\sum_{k=1}^{n} \mathbb{1}_{\{y_k>0\}}$ is an estimate of M. In a few sub-acquisitions (the 3rd and 16th), incident ions lead to no detected SEs, resulting in an underestimation of M and thus an overestimation of η .
- (iv) Lambert quotient mode. The LQM estimator (22) adjusts the QM estimator to compensate for the underestimation

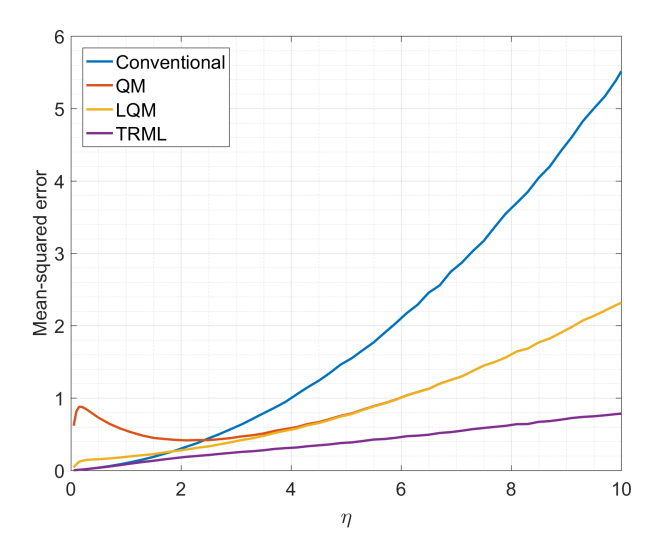


Figure 3: MSE comparison for Poisson-Poisson model in Section 2.1 as a function of η for conventional, quotient mode, Lambert quotient mode, and timeresolved maximum likelihood estimators with total dose $\lambda=20$ and n=100 sub-acquisitions.

of M, which yields $\hat{\eta}_{LQM} = W(-2.58 e^{-2.58}) + 2.58 \approx W(-0.1955) + 2.58 \approx 2.45$ after using a look-up table to evaluate W(-0.1955).

(v) Time-resolved maximum likelihood. The TRML estimator (24) is given by maximizing the likelihood $\prod_{k=1}^{n} P_Y(y_k; \eta, \lambda)$ over η . While the likelihood may be multimodal, it is typical for it to have an easily distinguished global maximum as shown in Figure 2b. Then $\hat{\eta}_{TRML}$ is the maximizing value of η , as depicted by the red star in Figure 2b.

Figure 3 shows MSE comparisons across η , by pseudorandom simulation, for the conventional, QM, LQM, and TRML estimators for $\lambda=20$ and n=100 sub-acquisitions. The curve for $\hat{\eta}_{\text{baseline}}$ matches the theoretical MSE expression in (6). QM has large MSE for low η values because low η leads to $\sum_{k=1}^n \mathbb{1}_{\{Y_k>0\}}$ being a very poor estimate of M. LQM thus improves significantly upon QM at low η . Estimates $\hat{\eta}_{\text{QM}}$ and $\hat{\eta}_{\text{LQM}}$ achieve convergence at moderate η values, while $\hat{\eta}_{\text{TRML}}$ uniformly achieves the lowest MSE amongst all estimators across the full η range. This highlights the merits of time-resolved measurement and corresponding ML estimation. Moreover, TR measurements and relatively simple processing like QM or LQM also yield moderate MSE improvements.

We also compare the four implementable estimators in a simulated imaging experiment. Figure 4a shows the "Modified Shepp–Logan phantom" provided by the Matlab phantom command, at size 256×256 , scaled to give ground truth SE yield values in the interval [2, 8], as suggested in [26]. Figures 4b–4e show image formation results for a total dose of $\lambda=20$ split evenly over n=100 sub-acquisitions. Consistent with the results in Figure 3, the TRML method achieves an MSE reduction by a factor of 2.6 as compared to the conventional, with the QM and LQM methods achieving substantial but lesser improvements. An alternative way to demonstrate the improve-

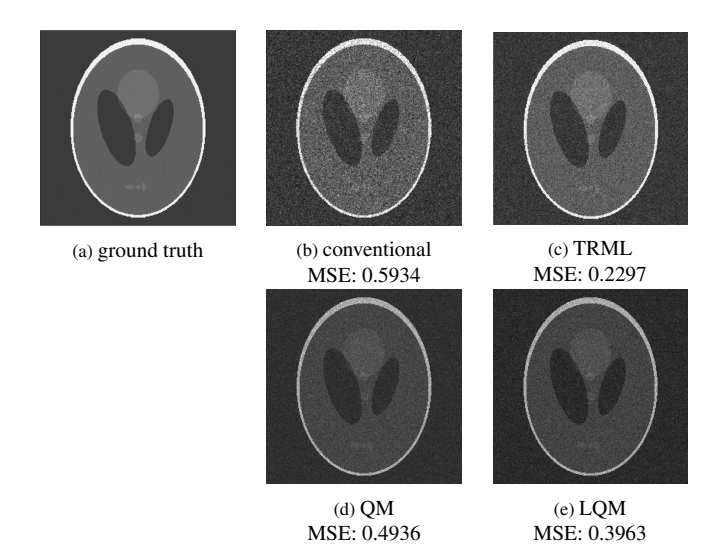


Figure 4: Simulated HIM experiment under Poisson–Poisson (direct electron detection) model in Section 2.1. Measurement is with total dose $\lambda=20$ split evenly over n=100 sub-acquisitions. (a) Ground truth image with mean secondary electron yield η in [2, 8]. (b) Conventional HIM image. (c) Pixelwise TRML estimates (24). (d) Quotient mode estimates (20). (e) Lambert quotient mode estimates (22). These results do not use spatial regularization.

ment due to TR measurement is through a dose reduction for fixed image quality. For example, TRML achieves a slightly lower MSE than the conventional reconstruction in Figure 4b with a dose of only 10 ions per pixel [27, Fig. 4d].

4. Hierarchical compound models

The model introduced in Section 2.1 assumes direct secondary electron counting, so that the number of SEs is the final readout of the device. In current HIM instruments, the output is more indirect. We now discuss some plausible models for the SE detection process and show that simulations continue to suggest substantial advantages for time-resolved measurement.

4.1. Poisson-Poisson-Normal

In a typical HIM instrument, SEs emitted due to ion-sample interaction are accelerated towards a phosphor scintillator plate by an electric field. Photons generated as a result of SE-scintillator interaction are amplified by a photomultiplier tube (PMT) and subsequently converted into an electrical current [28]. There is high degree of randomness in the scintillator and the PMT response [29], both of which cause randomness in the output current.

As one possible model with only two additional parameters, one could model the contribution to the final measurement from each detected SE as being normally distributed. Specifically, suppose the measured output current due to the jth SE is normal with mean c_1 and variance c_2 , i.e., $Z_j \sim \mathcal{N}(c_1, c_2)$. Then, the observation model at one pixel becomes

$$U = \sum_{j=1}^{Y} Z_j,\tag{25}$$





(a) Conventional $\lambda = 20$, MSE: 1.053

(b) time-resolved ML $\lambda = 20$, MSE: 0.562

Figure 5: Simulated HIM experiment for Quantized Poisson–Poisson–Normal model in Section 4.2 when $\lambda=20$, $c_1=10$, and $c_2=200$: (a) Conventional HIM image. (b) Pixelwise TRML estimates computed from n=100 time-resolved measurements. These results do not use spatial regularization.

where Y is the number of SEs. Combining the normal distribution with the Neyman Type A distribution in (2) gives the following probability density function (PDF) for U:

$$f_U(u; \eta, \lambda, c_1, c_2) = \sum_{y=1}^{\infty} \frac{1}{\sqrt{2\pi c_2 y}} \exp\left(-\frac{(u - c_1 y)^2}{2c_2 y}\right) P_Y(y; \eta, \lambda).$$
(26)

Under (26), the ML estimate of η , from n short acquisitions, becomes:

$$\hat{\eta}_{\text{TRML}} = \underset{\eta}{\text{arg max}} f_{U_1, \dots, U_n}(u_1, \dots, u_n; \eta, \lambda, c_1, c_2),$$
 (27)

where

$$f_{U_1,\ldots,U_n}(u_1, \ldots, u_n; \eta, \lambda, c_1, c_2) = \prod_{k=1}^n f_U(u_k; \eta, \lambda, c_1, c_2).$$

4.2. Quantized Poisson-Poisson-Normal

While the Poisson–Poisson–Normal model of Section 4.1 attempts to account for randomness in the scintillator and PMT responses, several aspects of a typical HIM instrument are not modelled. In particular, (26) allows negative measurements and the analog-to-digital conversion (ADC) to map output current into an 8-bit gray scale value is unmodelled. Assuming analog gains are set to avoid ADC overload, both of these effects can be accounted for by rounding the measurement to its nearest nonnegative integer. (Overload could be accounted for similarly.) Consequently, the PMF for the observed output $\widetilde{U} \in \mathbb{N}$ for each pixel is then:

$$P_{\widetilde{U}}(\widetilde{u}; \eta, \lambda, c_1, c_2) = \frac{\int_{\widetilde{u} - \frac{1}{2}}^{\widetilde{u} + \frac{1}{2}} f_U(u; \eta, \lambda, c_1, c_2) du}{\int_{-\frac{1}{2}}^{\infty} f_U(u; \eta, \lambda, c_1, c_2) du}.$$
 (28)

Note that the denominator in (28) normalizes the PMF to account for there being no negative measurements. The corresponding TRML estimate $\hat{\eta}_{TRML}$ under this new model can be written in an analogous fashion to (27).

Figure 5 shows the results of simulations for the same sample as in Figure 4. At the same dose of $\lambda = 20$, the MSEs are higher than in Figure 4, but substantial improvement from

time-resolved measurement is again demonstrated by a factor of 1.9. The reduced advantage relative to Figure 4 is attributable to the extra layer of randomness introduced by the scintillator and PMT. In addition, the discrepancy can be viewed as theoretical support for preferring direct secondary electron counting over other methods of electron detection.

5. HIM imaging results

5.1. Experiment details

Our methods were validated with data from a Zeiss ORION NanoFab HIM used to image a carbon-based defect on a silicon substrate. The instrument was used to collect 128 subacquisitions of the sample using a 0.1 pA beam current and 200 ns dwell time, resulting in low ion dose of 0.125 ions per pixel. The image of one typical sub-acquisition is shown in Figure 6a. In the first three columns of Figure 6, the scaling for display maps the range of the data linearly to the full black-to-white range, with 2% of pixels saturated at white. In the last two columns of Figure 6, absolute error values are shown for SE yield per incident ion with the scale indicated by the colorbars.

With the set of 128 sub-acquisitions, we can emulate conventional and time-resolved image formation for doses from 0.125 ions per pixel to 16 ions per pixel. Conventional image formation has no time resolution; this is emulated by summing the sub-acquisitions, as shown in Figures 6b and 6c. To take advantage of time-resolved acquisition, the Quantized Poisson–Poisson–Normal model of Section 4.2 was employed since the instrument does not use direct electron detection and its output at each pixel is a nonnegative integer. Hyper-parameters $c_1 = 5$ and $c_2 = 50$ were used without significant optimization. Results of pixel-by-pixel ML estimation under this model are shown in Figures 6g and 6h. With increasing ion dose (moving from second to third column of Figure 6), the image quality improves as expected. Results for other numbers of sub-acquisitions are presented in [27, Fig. 8].

5.2. Quantitative evaluation

With no ground truth image of the sample available, any accuracy claims are delicate. A proxy for ground truth is formed by taking the average of smoothed versions of the images produced using the conventional and TRML methods with all 128 sub-acquisitions. The smoothing operation is to replace a pixel by the average of its 8 neighbors; this is less likely to underestimate the errors than using a 9-pixel average that includes the pixel under consideration. The average of the two images and subsequent error image calculations are computed on a scale corresponding to SE yield, i.e., where values correspond to SEs detected per incident ion. The ground truth proxy is shown in Figure 6f. Absolute values of differences from the ground truth proxy are shown in Figures 6d, 6e, 6i, and 6j, zoomed in to the red boxes of the previous figures. It is apparent that the TRML method significantly reduces absolute error.

We define the MSE estimate \widehat{MSE} for an image as the average over all the pixels of the squared difference between the image and the ground truth proxy (Figure 6f); more conservative

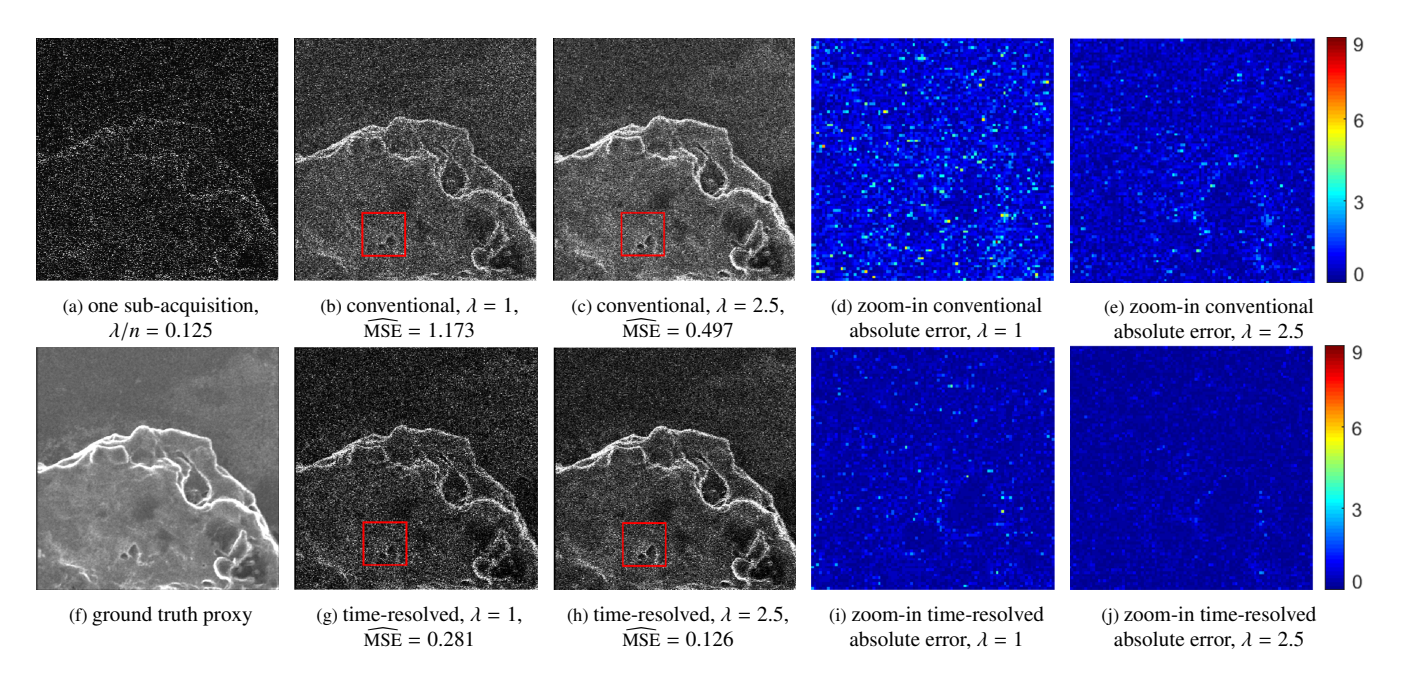


Figure 6: HIM experimental results for imaging a carbon-based defect on a silicon substrate sample. Results for our time-resolved method use the Quantized Poisson–Poisson–Normal compound model in Section 4.2 with $c_1 = 5$ and $c_2 = 50$. All images are produced pixel-by-pixel (i.e., without spatial regularization), and all errors are with respect to using (f) as a ground truth proxy. (a) A typical image from one sub-acquisition acquired with dose $\lambda/n = 0.125$ ions per pixel. (b) Conventional method using 8 sub-acquisitions. (c) Conventional method using 20 sub-acquisitions. (d) Absolute error of image shown in (b), zoomed in to the red square. (e) Absolute error of image shown in (c). (f) Ground truth proxy with dose $\lambda = 16$, formed by averaging results of smoothed time-resolved reconstruction and smoothed conventional reconstruction using 128 sub-acquisitions. The smoothed images are formed by replacing the center pixel with the average of 8 neighbor pixels around that center pixel. (g) Time-resolved method using 8 sub-acquisitions. (h) Time-resolved method using 20 sub-acquisitions. (i) Absolute error of image shown in (g). (j) Absolute error of image shown in (h). Comparing (b) and (g) (or (d) and (i)) shows MSE reduction by a factor of 4.17, and comparing (c) and (h) (or (e) and (j)) shows MSE reduction by a factor of 3.94.

quantitative comparisons are discussed in Section 5.3. These MSE estimates appear in the captions of Figure 6. Comparing Figures 6b and 6g shows a reduction of $\widehat{\text{MSE}}$ by a factor of 4.17, while comparing Figures 6c and 6h shows a reduction of $\widehat{\text{MSE}}$ by a factor of 3.94. By computing performance at more values of the total dose (i.e., more numbers of sub-acquisitions), one can interpret the improvement of the TRML method as a dose reduction for achieving a desired MSE [27].

5.3. Conservative error analysis

While we believe \widehat{MSE} to be a reasonable metric, we augment the comparison of \widehat{MSE} values with a more conservative approach.

Accumulating the sequence of 128 sub-acquisitions with conventional image formation creates a sequence of images, culminating in a $\lambda=16$ image which we refer to as $\hat{I}_{128}^{\text{conv}}$; similarly, the TRML method creates a sequence culminating in $\hat{I}_{128}^{\text{TRML}}$. The ground truth proxy defined in Section 5.2 and used to compute $\widehat{\text{MSE}}$ is the average of the 8-neighbor smoothed versions of $\hat{I}_{128}^{\text{TRML}}$ and $\hat{I}_{128}^{\text{conv}}$. Comparing a conventionally formed image to smoothed $\hat{I}_{128}^{\text{conv}}$ likely underestimates its error, so we call the average squared difference MSE⁻; comparing it to smoothed $\hat{I}_{128}^{\text{TRML}}$ likely overestimates its error, so we call the average squared difference MSE⁺. Conversely, comparing an image formed with the TRML method to smoothed $\hat{I}_{128}^{\text{TRML}}$ likely underestimates its error, so we call the average squared difference MSE⁻; comparing it to smoothed $\hat{I}_{128}^{\text{ronv}}$ likely overestimates

its error, so we call the average squared difference MSE⁺. The square roots of these values are called RMSE⁻ and RMSE⁺ and are shown along with $\widehat{\text{MSE}}^{1/2}$ in Figure 7.

While MSE⁻ and MSE⁺ are not rigorously lower and upper bounds to the MSE, they strengthen the evidence that the TRML method provides a substantial improvement. For example, we see that for ion doses up to 9, MSE⁺ for the TRML method is lower than MSE⁻ for the conventional method.

6. Discussion

The main contribution of this paper is to introduce the idea that a set of low-dose focused ion beam microscope measurements can be substantially more informative than a single measurement with the same total dose. We refer to the acquisition of the set of low-dose measurements as "time-resolved measurement" because it can be realized by keeping beam current and total dwell time unchanged, while dividing the dwell time into short time segments.

Our demonstrations of the potential of TR measurements take a few forms. For a Poisson-Poisson model (Section 2.1) that serves as an abstract model for FIB measurement with direct detection of secondary electrons, we used normalized Fisher information to demonstrate that low-dose measurements are the most informative per incident ion (comparison of (13) and (14)); furthermore, we used simulations to demonstrate that ML estimation achieves performance improvement consistent

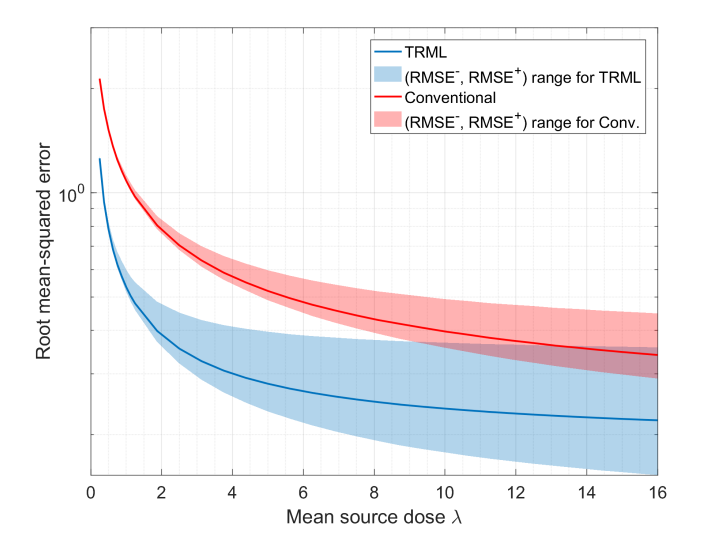


Figure 7: Estimated root mean-squared error $\widehat{MSE}^{1/2}$ (see Section 5.2) as a function of mean source dose λ for conventional (red) and time-resolved sensing (blue) methods. Also shown are the ranges (RMSE⁻, RMSE⁺) (see Section 5.3) intended to allow more conservative comparisons.

with the Fisher information increase (Figure 4). Indirect detection of secondary electrons can be modeled as well (Section 4). While analysis is made more complicated by these hierarchical models, imaging simulations indicate that substantial improvements are still possible (Figure 5). Experiments with HIM data used a Quantized Poisson–Poisson–Normal model (Section 4.2) and demonstrated the advantage of TR measurements and processing, even without direct electron counting (Figures 6 and 7).

Appendix A. Neyman Type A distribution of the number of secondary electrons

We wish to derive the PMF of Y in (1), where $M \sim \operatorname{Poisson}(\lambda)$ and $X_i \sim \operatorname{Poisson}(\eta)$ for each i. Since the sum of a deterministic number of Poisson random variables is a Poisson random variable, given M = m, Y is a Poisson random variable with mean $m\eta$. The PMF of Y can now be derived by marginalizing the joint PMF of Y and M over M:

$$\begin{split} P_{Y}(y) &= \sum_{m=0}^{\infty} P_{Y,M}(y,m) \stackrel{(a)}{=} \sum_{m=0}^{\infty} P_{Y|M}(y \mid m) \, P_{M}(m) \\ &\stackrel{(b)}{=} \sum_{m=0}^{\infty} \frac{e^{-m\eta} (m\eta)^{y}}{y!} \frac{e^{-\lambda} \lambda^{m}}{m!} = \frac{e^{-\lambda} \eta^{y}}{y!} \sum_{m=0}^{\infty} \frac{(\lambda e^{-\eta})^{m} m^{y}}{m!}, \end{split}$$

where (a) follows from the multiplication rule; and (b) from substituting Poisson PMFs. This verifies (2). The mean in (3) and variance in (4) follow from the laws of total expectation and of total variance, each applied with conditioning on M.

Declarations of interest

The authors declare no competing financial interests.

Author contributions

KKB and VKG conceived of time-resolved measurement in FIB microscopy. MP, JMB, and VKG derived the mathematical results. MP wrote software for image formation and completed all numerical experiments. MP, JMB, and VKG wrote the manuscript. All authors edited the manuscript.

Acknowledgments

The authors thank John Notte and Deying Xia of Carl Zeiss Microscopy LLC for enlightening discussions and experimental data and thank Akshay Agarwal and Emily Toomey for comments on an earlier manuscript.

Funding: This material is based upon work supported in part by the US National Science Foundation under Grant No. 1422034 and Grant No. 1815896.

References

- [1] D. McMullan, Scanning electron microscopy 1928–1965, Scanning 17 (3) (1995) 175–185.
- [2] M. Minsky, Memoir on inventing the confocal scanning microscope, Scanning 10 (4) (1988) 128–138.
- [3] W. Denk, J. H. Strickler, W. W. Webb, Two-photon laser scanning fluorescence microscopy, Science 248 (4951) (1990) 73–76.
- [4] E. W. Müller, T. T. Tsong, Field Ion Microscopy: Principles and Applications, American Elsevier, 1969.
- [5] B. W. Ward, J. A. Notte, N. P. Economou, Helium ion microscope: A new tool for nanoscale microscopy and metrology, J. Vac. Sci. & Technol. B 24 (6) (2006) 2871–2874.
- [6] M. Peng, J. Murray-Bruce, K. K. Berggren, V. K. Goyal, Source shot noise mitigation in scanned beam microscopy, in: Proc. 62nd Int. Conf. Electron, Ion, Photon Beam Technologies and Nanofabrication, Rio Mar, PR, 2018.
- [7] J. C. H. Spence, Diffractive (lensless) imaging, in: Science of Microscopy, Springer, 2007, pp. 1196–1227.
- [8] N. P. Economot, J. A. Notte, W. B. Thompson, The history and development of the helium ion microscope, Scanning 34 (2) (2012) 83–89.
- [9] M. S. Joens, C. Huynh, J. M. Kasuboski, D. Ferranti, Y. J. Sigal, F. Zeitvogel, M. Obst, C. J. Burkhardt, K. P. Curran, S. H. Chalasani, et al., Helium ion microscopy (HIM) for the imaging of biological samples at subnanometer resolution, Sci. Rep. 3 (2013) 3514.
- [10] R. Ramachandra, B. Griffin, D. Joy, A model of secondary electron imaging in the helium ion scanning microscope, Ultramicroscopy 109 (6) (2009) 748–757.
- [11] M. Schürmann, N. Frese, A. Beyer, P. Heimann, D. Widera, V. Mönkemöller, T. Huser, B. Kaltschmidt, C. Kaltschmidt, A. Gölzhäuser, Helium ion microscopy visualizes lipid nanodomains in mammalian cells, Small 11 (43) (2015) 5781–5789.
- [12] V. Castaldo, C. W. Hagen, P. Kruit, Simulation of ion imaging: Sputtering, contrast, noise, Ultramicroscopy 111 (8) (2011) 982–994.
- [13] V. Castaldo, C. W. Hagen, P. Kruit, E. Van Veldhoven, D. Maas, On the influence of the sputtering in determining the resolution of a scanning ion microscope, J. Vac. Sci. & Technol. B 27 (6) (2009) 3196–3202.
- [14] J. Orloff, L. W. Swanson, M. Utlaut, Fundamental limits to imaging resolution for focused ion beams, J. Vac. Sci. & Technol. B 14 (6) (1996) 3759–3763.
- [15] V. Castaldo, C. Hagen, B. Rieger, P. Kruit, Sputtering limits versus signal-to-noise limits in the observation of sn balls in a ga+ microscope, Journal of Vacuum Science & Technology B: Microelectronics and Nanometer Structures Processing, Measurement, and Phenomena 26 (6) (2008) 2107–2115.
- [16] D. Fox, Y. B. Zhou, A. O'Neill, S. Kumar, J. J. Wang, J. N. Coleman, G. S. Duesberg, J. F. Donegan, H. Z. Zhang, Helium ion microscopy of graphene: Beam damage, image quality and edge contrast, Nanotechnology 24 (33) (2013) 335702.

- [17] R. Livengood, S. Tan, Y. Greenzweig, J. Notte, S. McVey, Subsurface damage from helium ions as a function of dose, beam energy, and dose rate, J. Vac. Sci. & Technol. B 27 (6) (2009) 3244–3249.
- [18] J. Cazaux, Calculated influence of work function on SE escape probability and secondary electron emission yield, Applied Surface Science 257 (3) (2010) 1002–1009.
- [19] F. Timischl, M. Date, S. Nemoto, A statistical model of signal–noise in scanning electron microscopy, Scanning 34 (3) (2012) 137–144.
- [20] J. Neyman, On a new class of "contagious" distributions, applicable in entomology and bacteriology, Ann. Math. Statist. 10 (1) (1939) 35–57.
- [21] M. C. Teich, Role of the doubly stochastic Neyman type-A and Thomas counting distributions in photon detection, Appl. Optics 20 (14) (1981) 2457–2467.
- [22] J. W. Ward, R. L. Kubena, R. J. Joyce, An ion counting apparatus for studying the statistics of ion emission from liquid metal ion sources, J. Vac. Sci. & Technol. B 9 (6) (1991) 3090–3094.
- [23] S. M. Kay, Fundamentals of Statistical Signal Processing: Estimation Theory, Prentice-Hall, Inc., Upper Saddle River, NJ, USA, 1993.
- [24] J. A. Notte, Imaging with helium ions A new detector regime with new challenges and new opportunities, presented at the American Vacuum Society 60th Int. Symp. Exhibit., October 31 (no proceedings) (2013).
- [25] R. M. Corless, G. H. Gonnet, D. E. G. Hare, D. J. Jeffrey, D. E. Knuth, On the Lambert W function, Advances in Computational Mathematics 5 (1) (1996) 329–359.
- [26] J. Notte, R. Hill, S. McVey, L. Farkas, R. Percival, B. Ward, An introduction to helium ion microscopy, Microscopy and Microanalysis 12 (S02) (2006) 126–127.
- [27] M. Peng, J. Murray-Bruce, K. K. Berggren, V. K. Goyal, Source shot noise mitigation in focused ion beam microscopy by time-resolved measurement, arXiv:1906.03285v1 (Jun. 2019).
- [28] J. Notte, B. Ward, N. Economou, R. Hill, R. Percival, L. Farkas, S. McVey, An introduction to the helium ion microscope, in: AIP Conference Proceedings, Vol. 931, AIP, 2007, pp. 489–496.
- [29] T. Hakamata, et al., Photomultiplier Tubes: Basics and Applications, 3rd Edition, Hamamatsu Photonics K. K., 2007.